



# Preparation, characterization, and photocatalytic performance of atmospheric plasma-sprayed $\text{TiO}_2/\text{Al}_2\text{O}_3$ coatings on glass substrates

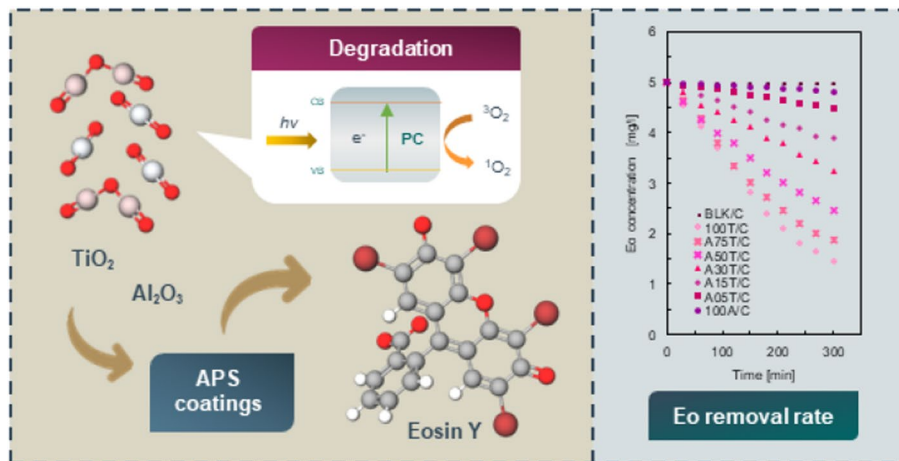
Alicja Duda<sup>1,3</sup> · Bartosz Kopyciński<sup>2,3</sup> · Łukasz Hawelek<sup>1</sup> · Marcin Lis<sup>1</sup> · Grzegorz Muzia<sup>1</sup> · Adriana Wrona<sup>1</sup>

Received: 25 September 2023 / Revised: 8 March 2024 / Accepted: 28 March 2024  
© The Author(s) 2024

## Abstract

Conventional methods for wastewater treatment are not always efficient in persistent organic pollutant degradation processes. Therefore, low-cost and effective methods of their removal from sewage are constantly sought. This study presents an attempt to fabricate thermally sprayed ceramic coatings on glass and their characterization. Granulation of  $\text{TiO}_2$ ,  $\text{Al}_2\text{O}_3$ , and their blends in different mass ratios was done. Assessment of actual density and specific surface area was performed, and  $\text{TiO}_2$ ,  $\text{Al}_2\text{O}_3$ , and  $\text{TiO}_2/\text{Al}_2\text{O}_3$  were then used as a coating material for the deposition on glass substrates in atmospheric plasma spraying. Surface analysis of coatings was done by evaluating their roughness and wettability. Both powder and coatings samples were characterized using the X-ray diffraction method and scanning electron microscopy. The photocatalytic activity was estimated in the Eosin Y degradation process under UV light. UV–Vis spectroscopy was applied to observe the changes in the dye concentration. Additional tests for color measurements before and after photodegradation were carried out using a sphere spectrophotometer in CIELab color space. Particle size distribution was examined for the powder samples after the granulation and  $d_{50}$  was stated at 48.42–63.28  $\mu\text{m}$ . Characterization of coatings via roughness measurements showed the average roughness of a surface equal to 4.90–9.65  $\mu\text{m}$ . Moreover, most of the coatings appeared to be hydrophobic with water contact angles between  $100^\circ$  and  $130^\circ$ . All of the coatings showed Eosin Y degradation ability and the highest efficiency was reached for 100T/C, A75T/C, and A50T/C samples and stated at 71%, 62%, and 51%, respectively.

## Graphical abstract



**Keywords** Oxide ceramics · Organic dye photodegradation · Thermally sprayed coatings · Atmospheric plasma spraying · Functional coatings

Extended author information available on the last page of the article

## 1 Introduction

The organic pollutants produced during various technological processes in the chemical, food, textile, or pharmaceutical industries have contributed to environmental pollution for many years. Among these contamination types, organic dyes widely used in many scientific and industrial disciplines should be mentioned [1]. Today, the production rate of dyes on a global scale is almost 800 thousand per year, and the increase in production and costs in the dyes market in the next 6 years is expected to increase by as much as 5% [2]. Although the development of the area of coloring substances leads to improving their production technologies, it is also a source of toxic and often difficult-to-remove pollutants, which can cause extensive water or soil pollution. Moreover, classic wastewater treatment methods are usually inefficient enough to deal with substances such as organic dyes [3]. Hence, there are many interesting, unconventional proposals for the removal of organic water pollutants, such as technologies based on processes of adsorption [4], sedimentation [5], filtration [6], encapsulation [7], microbial degradation [8] or oxidation [9], and photocatalytic processes [10]. This article focuses on photocatalytic degradation, which is classified as one of the advanced oxidation processes (AOP) [11]. In these processes, organic compounds are decomposed into simple inorganic molecules and ions such as  $\text{CO}_2$ ,  $\text{H}_2\text{O}$  molecules, and  $\text{NO}_3^-$ ,  $\text{PO}_4^{3-}$ , or  $\text{CO}_3^{2-}$  ions [12]. One of the most frequently discussed groups of photocatalysts is inorganic semiconductors such as metal oxides (i.e.  $\text{TiO}_2$ ,  $\text{Fe}_2\text{O}_3$ ,  $\text{ZnO}$ ,  $\text{SnO}_2$ ,  $\text{ZrO}_2$ ,  $\text{WO}_3$ ) or salts (i.e.  $\text{InS}_3$ ,  $\text{CdS}$ ,  $\text{FeSe}$ ,  $\text{CuSe}$ ) and others (i.e.  $\text{Ta}_3\text{N}_5$ ,  $\text{g-C}_3\text{N}_4$ ,  $\text{NaYbF}_4$ ) [13]. These can be used not only for dyes degradation but also for other pollutants such as phenols, drugs, pesticides, or paint components [11]. Among semiconductor metal oxides applied as photocatalysts,  $\text{TiO}_2$  is widely used. This is mainly because of its excellent ability to catalyze light-activated processes, high thermal and chemical stability, or low toxicity [14]. Two crystal phases of  $\text{TiO}_2$ , anatase, and rutile, are commonly used in photocatalytic reactions [15]. Although anatase has a higher catalytic activity than rutile, both are considered significant mediums in photocatalytic processes [16]. Rutile has better functional properties, such as Mohs hardness (6.0–6.5 for rutile and 5.5–6.0 for anatase) or better thermal resistance than anatase, which

**Table 1** Properties of  $\text{TiO}_2$  and  $\text{Al}_2\text{O}_3$  as delivered

Powder	$S$ [ $\text{m}^2/\text{g}$ ]	$\rho$ [ $\text{g}/\text{cm}^3$ ]	$\bar{d}$ [nm]
$\text{TiO}_2$ AreOxide P25	$51.62 \pm 0.12$	$4.42 \pm 0.02$	$26.30 \pm 0.26$
$\text{Al}_2\text{O}_3$ AreOxide AluC	$97.58 \pm 0.15$	$3.35 \pm 0.02$	$18.36 \pm 0.20$

**Table 2** Contents of prepared samples

Sample	$\text{Al}_2\text{O}_3$ [%]	$\text{TiO}_2$ [%]	PVP [%]
100T/P	0	100	1.0
A75T/P	25	75	1.0
A50T/P	50	50	1.5
A30T/P	70	30	2.0
A15T/P	85	15	2.5
A05T/P	95	05	3.0
100A/P	100	0	3.0

determines its good behavior under extreme conditions [17]. In materials engineering, attempts to obtain products with better performance properties are constantly undertaken, and the idea of improving composites is also reflected in the semiconductor photocatalysts research area. Here, solutions based on oxide ceramics blends can be distinguished, i.e., the combination of  $\text{TiO}_2$  and  $\text{Al}_2\text{O}_3$  characterized by high hardness and strength and excellent chemical resistance [18]. The economic aspect is also essential, and though there are many types of  $\text{TiO}_2$ -based products on the market, their price can still be relatively high. The selection of cheaper additives—for example,  $\text{Al}_2\text{O}_3$ —can significantly reduce production costs [19].

Another worth mentioning matter in the case of photocatalysts for water disinfection is their limited use when solubilized in the homogeneous mixture or added in the form of powders to the purifying solution. Although photocatalysts are usually the most efficient in such systems, they can also become challenging to separate impurities. New methods of applying catalysts to solid substrates are being sought, and a significant development in this field has been done over the past 20 years. Technologies for producing coatings or thin films on solid surfaces, including spin-coating [20], cold-spraying [21], physical [22], and chemical [23] vapor deposition or different methods of thermal spraying [24], are of great interest in this area. Among the thermal spray techniques, the most frequently used in the fabrication of photocatalytic coatings are high-velocity oxygen-fuel (HVOF) [25] or atmospheric plasma spraying (APS) [26], and in recent years suspension plasma spraying (SPS)—which it is predominantly suitable for nanometric feedstock spraying—has been increasingly mentioned [27]. Immobilization of photocatalysts can also be carried out by their encapsulation in the polymer matrix [28], addition to paints [29], or deposition by chemical surface modification [30]. A wide range of coating solutions and other methods of immobilizing photocatalysts enable their reusability, lowering exploitation costs. Some of these techniques are used not only for the fabrication of coatings for photocatalytic applications but also for their additional advantages, such as,

among many others, anticorrosive activity, wear resistance, or thermal stability [31].

This paper presents research on the preparation and characterization of ceramic coatings fabricated via the atmospheric plasma spray method. For this purpose, nanometric powders of  $\text{TiO}_2$ ,  $\text{Al}_2\text{O}_3$ , and  $\text{TiO}_2/\text{Al}_2\text{O}_3$  blends were used. Physical properties, i.e. actual density, specific surface area, average particle size, and particle size distribution of the obtained blends, were determined, and the phase composition was analyzed by means of X-ray diffractometry (XRD). The samples were imaged by scanning electron microscopy (SEM). Then, APS coatings on glass substrates were obtained and analyzed by XRD analysis and SEM imaging. Properties such as roughness and wettability were also determined. The photocatalytic ability of the obtained coatings containing  $\text{TiO}_2$ ,  $\text{Al}_2\text{O}_3$ , and  $\text{TiO}_2/\text{Al}_2\text{O}_3$  were tested based on the degradation processes of Eosin Y (Eo) in water solution. Additionally, in order to evaluate the photocatalytic performance of raw coating materials before the APS process, degradation of Eo was also performed for powder samples. The color measurements of powders and coatings were carried out before and after the processes.

Most commonly, especially in industrial practice, thermally sprayed coatings were mainly fabricated with the use of micrometric, non-treated factory  $\text{TiO}_2$  and  $\text{Al}_2\text{O}_3$  as feedstock materials. However, their physical and functional properties differ significantly from those of nanopowders. In the scientific literature, numerous reports on the use of submicrometric and nanometric powders used as feedstock for photocatalytic thermal sprayed coatings can be found. The use of nanopowder suspensions [27] or solutions [32] in SPS techniques [33] is currently one of the most often discussed in this area.

As part of this research, it was possible to obtain micrometric powders from nano- $\text{TiO}_2$  and  $\text{Al}_2\text{O}_3$  using a simple and non-invasive granulation technique with a polymeric binder. This, in turn, provided an increase in powders flowability (which is important in APS deposition processes) while maintaining the initial properties of raw materials.

**Table 3** Spraying parameters

Parameter	Value
Gas flow rate [L/min]	
Hydrogen	14
Argon	41
Carrier gas	4.50
Arc current [A]	600
Nozzle diameter [mm]	1.80
Spraying distance [mm]	145
Wheel speed of powder feeder [rpm]	4
Speed of movement (X) [m/s]	0.40
Speed of movement (Y) [m/s]	4.15

## 2 Experimental

### 2.1 Materials

Powder samples were prepared with the use of the following materials: titanium dioxide  $\text{TiO}_2$  (AreOxide P25, Evonic Industries), aluminum oxide  $\text{Al}_2\text{O}_3$  (AreOxide AluC, Evonic Industries), polyvinylpyrrolidone PVP (K12, Acros Organics). Properties for powders as delivered are presented in Table 1. The dye photodegradation process was done on the example of Eo (PolAura) in an aqueous solution.

### 2.2 Powder sample preparation

The samples were prepared by granulating different mass ratios of  $\text{TiO}_2$  and  $\text{Al}_2\text{O}_3$  (Table 2) by adding a polymeric binder PVP using an Eirich EL1 laboratory mixer. Before the granulation process, PVP was added to the  $\text{Al}_2\text{O}_3$  powder and then subjected to mixing at 500 rpm for 40 s and 1500 rpm for 60 s.  $\text{TiO}_2$  fractions were added gradually and mixed at increasing mixer speeds (from 600 to 3000 rpm). The obtained granules were allowed to air-dry overnight. After this, the powder samples were sieved through 220  $\mu\text{m}$  sieves and dried at 80 °C for 4 h. The increasing ratio of PVP in the prepared mixtures was applied because of the nature of the powders as delivered. The finer the powder is, the more difficult it is to granulate, so with an increasing  $\text{Al}_2\text{O}_3$  ratio, there was a need for a more significant amount of binder.

### 2.3 Actual density and specific surface area

The actual density  $\rho$  of the powder samples was measured by the gas pycnometry method using the Micromeritics AccuPyc 1340 II pycnometer. Measurements were performed at room temperature in a sample chamber with a volume of 10  $\text{cm}^3$  and helium as an inert gas. Results for density were obtained for 50-cycle repetitions.

The determination of the specific surface area  $S$  was carried out on a Micromeritics Gemini 2360 apparatus. The measuring range was 0.01  $\text{m}^2/\text{g}$  for the specific surface and 0.1–300  $\text{m}^2$  for the total surface. The samples were dried overnight at 105 °C under a nitrogen atmosphere to remove impurities and moisture. The measurements were performed in the  $P/P_0$  range of 0.05–0.30.

Based on the abovementioned measurements, the average particle size  $\bar{d}$  of obtained powders was determined. Calculations were done with the use of the equation:

$$\bar{d} = \frac{6 \cdot 10^3}{\rho \cdot S},$$

where  $\rho$ —actual density [ $\text{g}/\text{cm}^3$ ] and  $S$ —specific surface area [ $\text{m}^2/\text{g}$ ].

## 2.4 Particle size distribution measurements

Particle size distribution (PSD) of TiO<sub>2</sub> and Al<sub>2</sub>O<sub>3</sub> powders after the granulation was determined via laser diffraction particle analysis using the NanoTec Analysette 22 apparatus from Fritsch. The measurements were carried out using the wet dispersion method in the measuring range of 0.1–504.48 μm in three repetitions. The Fraunhofer computational theory was applied in the analysis.

## 2.5 Fabrication of coatings

APS technique was applied to fabricate TiO<sub>2</sub>, Al<sub>2</sub>O<sub>3</sub>, and TiO<sub>2</sub>/Al<sub>2</sub>O<sub>3</sub> coatings. For this purpose, a spray system AP50 (Flame Spray Technologies) equipped with a torch F4 (Flame Spray Technologies) was employed. Quartz glass plates (AmekoTech dim. 190.0 × 80.0, thickness 4.0 mm) were used as a substrate. Before spraying, substrates were sandblasted with electrocorundum KOS Al<sub>2</sub>O<sub>3</sub> 99% F36 with a grain size of 600–500 μm at a pressure of  $5.5 \times 10^2$  kPa and an angle of 65°. The detailed parameters for the plasma spraying are presented in Table 3. The torch was maintained at a distance of 145 mm from the substrate. The powder samples were injected into the plasma flow via torch using gases with a flow stated at 14, 41, and 4.50 L/min for hydrogen, argon, and carrier gas, respectively. After the spraying, coatings were cooled at room temperature for 2 h and then purged with compressed air to remove dust and other impurities.

## 2.6 X-ray diffraction method

XRD analysis for both powders and coatings was performed by using a Rigaku MiniFlex600 diffractometer equipped with a vertical goniometer (radius of 150 mm), a one-dimensional silicon strip detector D/teX Ultra, CuKα radiation ( $\lambda = 1.54 \text{ \AA}$ ) with a Ni filter (for CuKβ filtering) operating

at a tube voltage of 40 kV and a tube current of 15 mA. The optical setup was in the Bragg–Brentano geometry with a variable divergence slit and a 10-mm receiving slit. Data for the phase identification were recorded in the  $2\theta$  range from 10° to 90° at 0.02° intervals and a scan speed of 5°/min. The diffraction pattern was analyzed to identify the crystalline phases using the PDXL2 software package. The relative intensity ratio (RIR) method was used to determine the rutile and anatase phase content in powders XRD using the PDXL 2 Version 2.2.2.0 Rigaku software package. In the RIR method, quantitative values are easily calculated using RIR values listed in a database from the integrated intensity of the maximum intensity curves of the examined components. This makes it possible to calculate quantitative values without plotting calibration curves.

## 2.7 Surface roughness

The geometric structure of the surface of the obtained coatings was evaluated using a portable roughness measuring instrument, Jenoptik Hommel-Etamic W20. Before the measurements, the coatings were treated under compressed air. The length traveled by the apparatus needle was 15 mm. Measurements for each sample were performed in

**Table 4** Powder samples' properties

Sample	$S$ [m <sup>2</sup> /g]	$\rho$ [g/cm <sup>3</sup> ]	$\bar{d}$ [nm]
100T/P	49.78 ± 0.28	3.61 ± 0.01	37.45 ± 0.32
A75T/P	55.27 ± 0.41	3.66 ± 0.01	33.73 ± 0.37
A50T/P	63.39 ± 0.28	3.30 ± 0.01	28.68 ± 0.19
A30T/P	79.09 ± 0.22	3.39 ± 0.01	22.39 ± 0.10
A15T/P	82.95 ± 0.22	3.33 ± 0.01	21.92 ± 0.10
A05T/P	84.17 ± 0.30	3.25 ± 0.01	21.91 ± 0.12
100A/P	86.47 ± 0.36	3.22 ± 0.01	21.56 ± 0.14

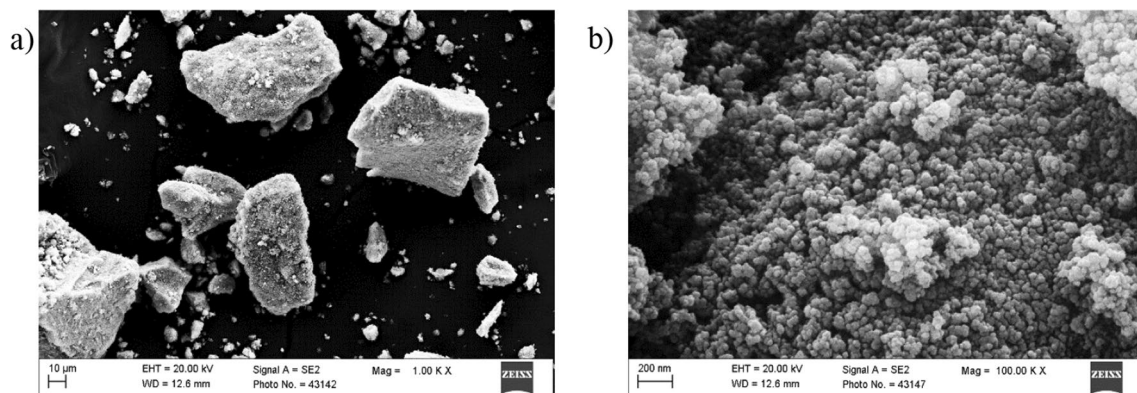


**Fig. 1** SEM images of **a** micrometric agglomerates and **b** powder nanoparticles on the example of the A50T/P sample

**Fig. 2** Frequency (a) and particle size (b) distribution plots for powder samples

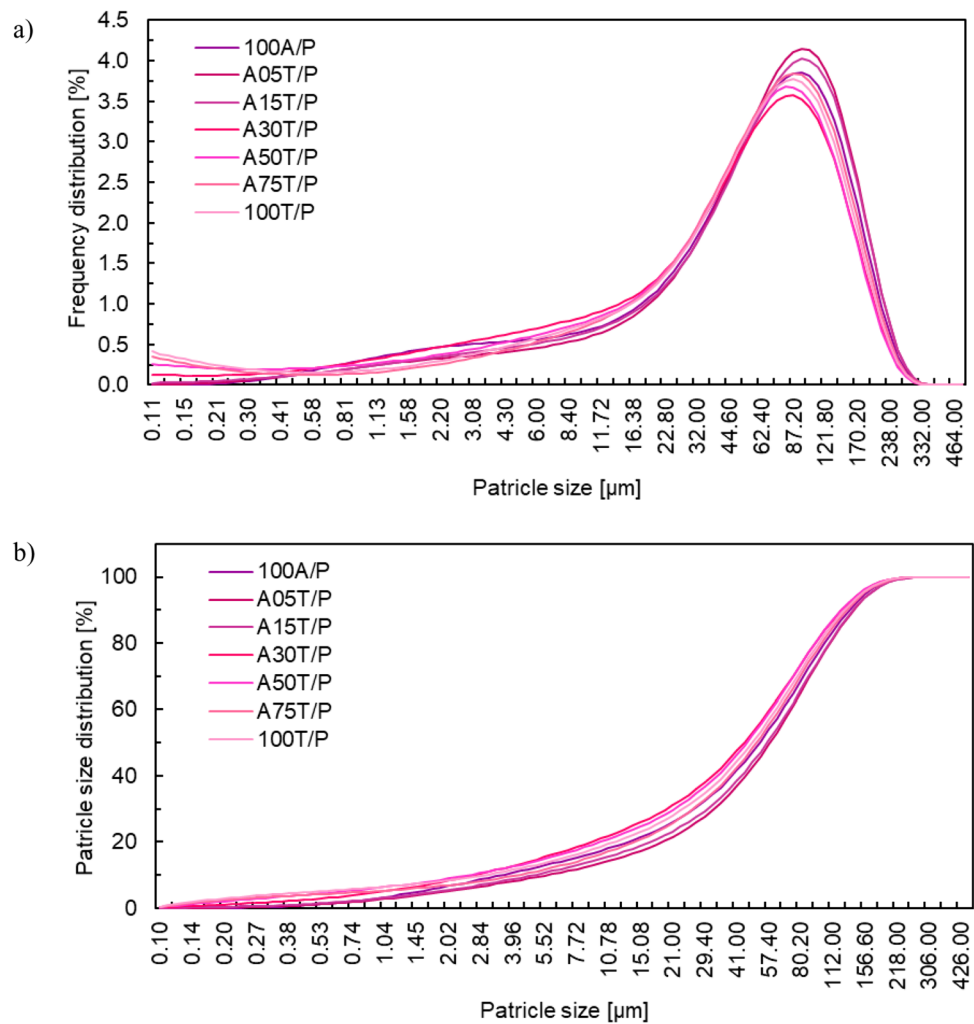


**Table 5** The points ( $d_{10}$ ,  $d_{50}$ ,  $d_{90}$ ) in the size distribution

Sample	$d_{10}$ [ $\mu\text{m}$ ]	$d_{50}$ [ $\mu\text{m}$ ]	$d_{90}$ [ $\mu\text{m}$ ]	Span value
100T/P	3.23	52.55	137.61	2.56
A75T/P	4.55	55.03	141.13	2.48
A50T/P	2.75	49.70	132.99	2.62
A30T/P	2.92	48.42	133.80	2.70
A15T/P	5.36	61.43	151.03	2.37
A05T/P	6.21	63.28	151.47	2.30
100A/P	3.87	56.74	144.82	2.48

ten repetitions. The analysis of the results was carried out based on ISO 4287 Geometrical product specifications—surface texture: profile method—terms, definitions, and surface texture parameters and ISO 4288 Geometrical product specifications—surface texture: profile method—principles and procedures for the assessment of the geometrical structure of the surface.

## 2.8 Wettability measurements

The ability of the sprayed coatings to be physically repelled or attracted by water molecules was determined by measuring the wettability with a Krüss DSA 100 goniometer under standard ISO 19403–2—Paints and varnishes—Wettability—Part 2: Determination of the surface free energy of solid surfaces by measuring the contact angle. Drops of deionized water with a surface tension of  $72.8 \text{ mJ/m}^2$  and a volume of approximately  $2 \mu\text{L}$  were deposited on the surface of the tested samples. The contact angles at the phase boundary were recorded sequentially. The test was performed in 5 replications per sample.

## 2.9 Light-activated dye degradation

Organic dye removal processes were performed with the use of powder samples and coatings as catalysts. For this purpose,  $5 \text{ mg/L}$  of aqueous Eo solution was prepared. Powders ( $1 \text{ g/L}$ ) or coated plates (dim.  $60.0 \times 80.0 \text{ mm}$ ) were placed

**Fig. 3** XRD patterns for TiO<sub>2</sub>/Al<sub>2</sub>O<sub>3</sub> powders samples and coatings. The diffraction peaks are identified and marked by defined symbols

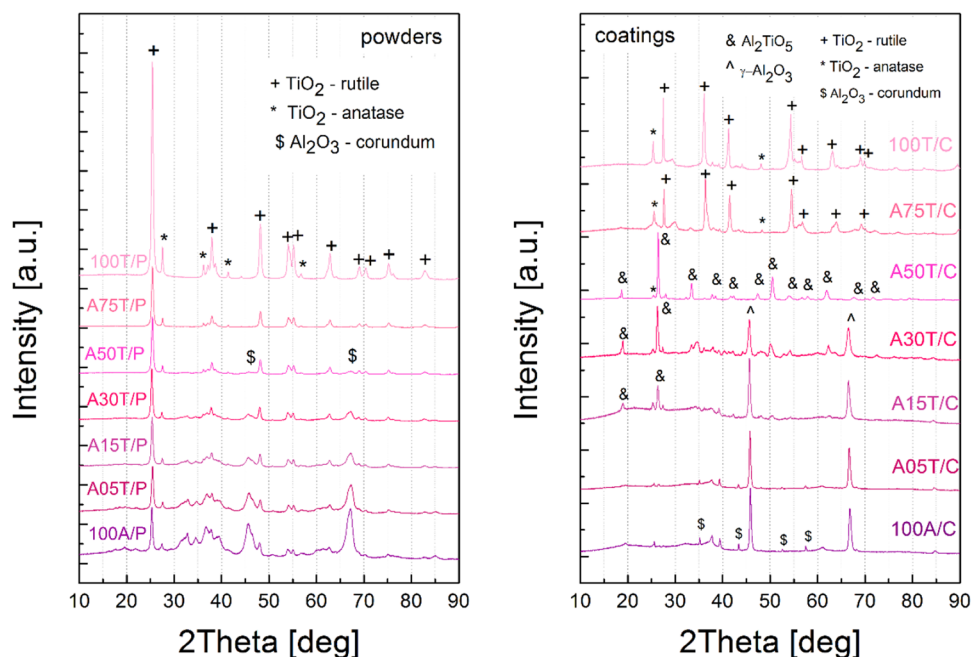


**Table 6** The calculated rutile and anatase phase content in studied powders based on the RIR method

Sample	Rutile [wt%]	Anatase [wt%]
100T/P	12.3	87.7
A75T/P	10.9	82.2
A50T/P	8.6	56.0
A30T/P	5.3	29.0
A15T/P	4.2	20.0
A05T/P	3.6	13.0
100A/P	–	–

**Table 7** Roughness parameters for fabricated coatings

Sample	R <sub>a</sub> [μm]	R <sub>z</sub> [μm]	R <sub>max</sub> [μm]
Glass substrate	0.06 ± 0.00	0.49 ± 0.04	1.04 ± 0.09
Sandblasted glass substrate	5.07 ± 0.41	36.11 ± 1.20	49.84 ± 5.01
100T/C	7.21 ± 0.60	41.94 ± 3.25	53.64 ± 8.26
A75T/C	9.45 ± 0.75	51.92 ± 1.56	66.58 ± 6.26
A50T/C	7.88 ± 0.92	45.17 ± 3.68	61.41 ± 9.80
A30T/C	7.19 ± 0.79	42.78 ± 4.55	54.04 ± 8.89
A15T/C	4.65 ± 0.59	34.42 ± 2.36	44.30 ± 4.41
A05T/C	9.63 ± 0.79	53.06 ± 2.70	68.65 ± 6.04
100A/C	4.91 ± 0.35	32.67 ± 1.11	39.07 ± 3.54

in the Eo solutions and exposed to UV light for 3 or 5 h, respectively. Solutions were stirred in the dark for 1 h before the light irradiation. UV lamp working at 254 nm were used as a source of light. Blank measurements were performed in which the dye solutions were exposed to light without using photocatalysts. All measurements were performed at room temperature. Changes in dye concentration were studied using a DU 640 Beckman UV–Vis spectrophotometer by observing the decrease in Eo absorbance at 514 nm.

**2.10 Color measurements**

The color of the powders in loose form and after being sprayed onto the substrate was determined using SP62 X-rite portable, handheld sphere spectrophotometer with a measuring geometry of d/8 according to ISO 7724-2 Paints and varnishes—Colorimetry—Part 2: Color measurement. The color coordinates in CIELab color space were calculated

(L\*—brightness, a\*—color from green to magenta, b\*—color from blue to yellow). The color difference ΔE before and after photocatalysis of powders and coatings was determined under ISO 7724-3 Paints and varnishes—Colorimetry—Part 3: Calculation of color differences. The calculations were made based on the following formula:

$$\Delta E = \sqrt{(\Delta L^*)^2 + (\Delta a^*)^2 + (\Delta b^*)^2}$$

**2.11 Scanning electron microscopy**

The microscopic observation was performed using LEO Gemini 1525 high-resolution scanning electron microscope with a resolution of 1.5 nm at a current voltage of 20 kV and equipped with an InLens detector. Before measurement, all analyzed samples were sputtered for 50 s with an Au

**Table 8** Contact angles for fabricated coatings

Sample	CA(M) [°]
100T/C	99.23 ± 35.10
A75T/C	125.12 ± 7.99
A50T/C	116.43 ± 8.67
A30T/C	109.94 ± 6.10
A15T/C	–
A05T/C	129.35 ± 7.02
100A/C	–

conductive layer in an Ar protective atmosphere using SEI supplies sputter coater. Before the analysis, both powders and coatings were dried overnight at 50 °C.

### 3 Results and discussion

#### 3.1 Powder characterization

In thermal spray technologies, the physical properties of the sprayed powders, such as particle size distribution, density, or flow rate, are important. Hence, nanometric TiO<sub>2</sub> and Al<sub>2</sub>O<sub>3</sub> powders were granulated with PVP as a binder. The presented SEM images of selected powder samples (Fig. 1) show nanoparticles' micrometric agglomerates, confirming the granulation efficiency.

The results obtained for *S* and  $\rho$  for prepared powder mixtures are 49.78–86.47 m<sup>2</sup>/g and 3.61–3.22 g/cm<sup>3</sup>, respectively. There are noticeable differences in values depending on the composition of a given mixture. And so, with the increase of the Al<sub>2</sub>O<sub>3</sub> content, the *S* values increase, and the  $\rho$  values decrease. This is due to the characteristics of the initial powders used in the granulation process. This relationship is also related to the calculation results of  $\bar{d}$ , which are almost 38 nm for 100T/P and 22 nm for 100A/P. Thus, it can be seen that with increasing Al<sub>2</sub>O<sub>3</sub> content, the calculated  $\bar{d}$  values are lower. The abovementioned results are listed in Table 4. It was confirmed that the obtained blends retained their nanometric properties despite the granulation process.

The successful granulation of TiO<sub>2</sub> and Al<sub>2</sub>O<sub>3</sub> nanoparticles was also confirmed by the results of PSD analysis. The obtained frequency and particle size distribution plots indicate similar distributions for all tested samples (Fig. 2). The particle diameters are stated between 2.75–6.21 μm for *d*<sub>10</sub>, 48.42–63.28 μm for *d*<sub>50</sub>, and 132.99–151.47 μm for *d*<sub>90</sub> (Table 5). Moreover, the distribution width was characterized by the calculation of the span values using the equation:  $(d_{90} - d_{10})/d_{50}$ . The obtained values were within the range of 2.30–2.70. The widest distribution was recorded for A30T/P and the narrowest for A05T/P.

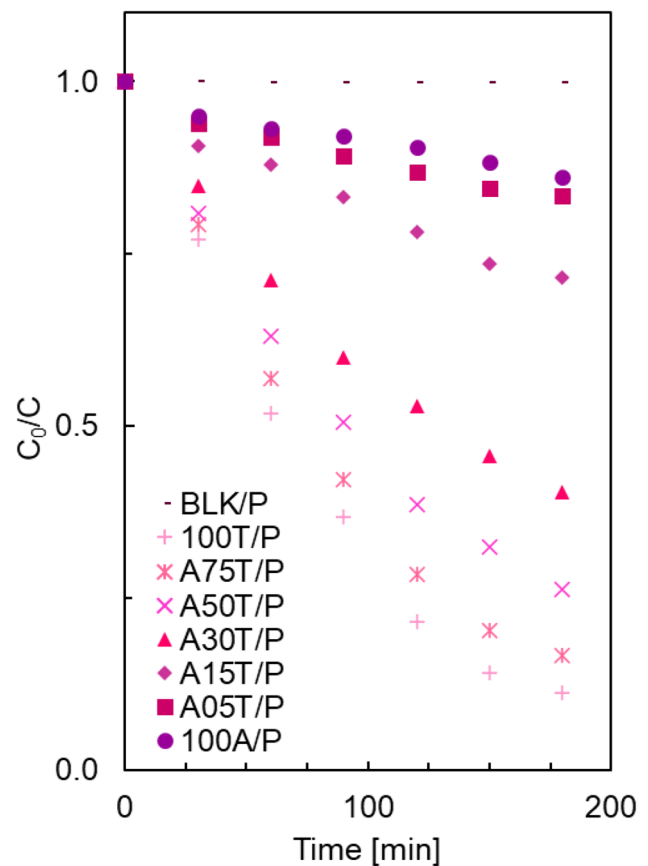


**Fig. 4** Decrease in Eo concentration in the reaction with powders

#### 3.2 X-ray diffraction method

The XRD patterns obtained for discussed powder samples and coatings are presented in Fig. 3. According to the technical data and laboratory tests of powders used in the granulation process [34], TiO<sub>2</sub> as delivered consists of almost 80% anatase and 20% rutile, while Al<sub>2</sub>O<sub>3</sub> consists in almost 99% of the α-Al<sub>2</sub>O<sub>3</sub> phase. The XRD analysis carried out in this study for the 100A/P, and 100T/P powder samples confirms the abovementioned reports—the dominant phases are anatase and α-Al<sub>2</sub>O<sub>3</sub>, respectively. In the case of

**Table 9** Eo degradation rate in the reaction with powders

Sample	Eo degradation rate [%]
100T/P	88.79
A75T/P	83.39
A50T/P	73.64
A30T/P	59.56
A15T/P	28.40
A05T/P	16.59
100A/P	13.83

the remaining powder samples—A75T/P, A50T/P, A30T/P, A15T/P, and A05T/P—obtained in the process of TiO<sub>2</sub> and Al<sub>2</sub>O<sub>3</sub> granulation, the anatase and rutile phases, as well as α-Al<sub>2</sub>O<sub>3</sub>, are also visible. The changes in the intensity of signals for these phases can be observed, which can confirm the differences in TiO<sub>2</sub> and Al<sub>2</sub>O<sub>3</sub> contents. The RIR determination of rutile and anatase phase content (Table 6) confirmed that anatase is in the predominant phase occurring in the samples. Its content increases with the increase in the share of TiO<sub>2</sub> in the sample’s composition. This, in turn, contributes to the improvement of photocatalytic performance—anatase is commonly considered a better catalyst than rutile [16]. In the case of samples 100T/P and 100T/C, some changes in the crystal phase from anatase to rutile are visible. Similarly, the phase transformation from α-Al<sub>2</sub>O<sub>3</sub> into γ-Al<sub>2</sub>O<sub>3</sub> between the samples 100A/P and 100A/C can be noted. These changes agree with studies dedicated to exploring the influence of thermal treatment on the crystalline structure of TiO<sub>2</sub> or Al<sub>2</sub>O<sub>3</sub>. It is proved that the rutile phase occurs during the calcination of TiO<sub>2</sub> at temperatures above 500 °C [35]. Whereas in the case of processing Al<sub>2</sub>O<sub>3</sub> at high temperatures, γ-Al<sub>2</sub>O<sub>3</sub> phase formation is preferred. Numerous studies have confirmed these findings on the deposition of TiO<sub>2</sub> and Al<sub>2</sub>O<sub>3</sub> by the APS method. During APS processes, the deposited raw material particles pass through the plasma stream, melt under the influence of extremely high temperatures, and then cool rapidly. Therefore, in most cases, rutile and γ-Al<sub>2</sub>O<sub>3</sub> are formed in thermally sprayed

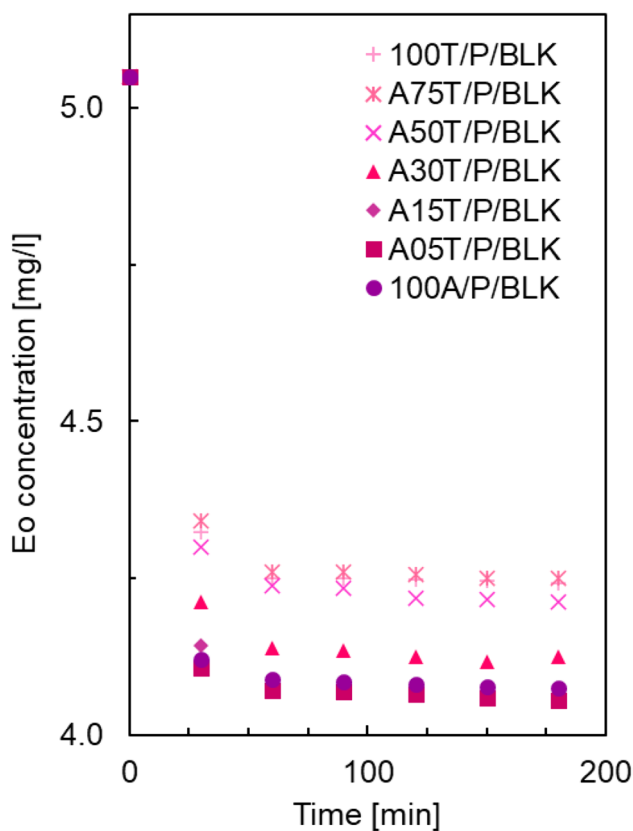


Fig. 5 Eo concentration in the dark measurements with the use of powders

**Table 10** Color measurement parameters for powders before and after Eo degradation (PC—post-photodegradation, BLK—blank measurements)

Sample	L*	a*	b*	Color	ΔE
100A/P	96.38	-0.47	0.24		-
100A/P/PC	96.17	8.57	0.94		9.07
100A/P/BLK	94.99	13.58	1.42		14.17
A05T/P	96.59	-0.59	0.48		-
A05T/P/PC	96.77	8.36	0.96		8.96
A05/P/BLK	94.20	13.87	1.64		14.57
A15T/P	97.29	-0.76	0.99		-
A15T/P/PC	97.01	7.09	2.14		7.94
A15T/P/BLK	94.61	13.41	2.13		14.47
A30T/P	97.29	-0.70	2.01		-
A30T/P/PC	97.23	5.56	1.23		6.31
A30T/P/BLK	95.60	12.61	2.07		13.42
A50T/P	97.86	-0.58	1.47		-
A50T/P/PC	97.50	2.10	2.60		2.93
A50T/P/BLK	95.29	11.85	3.00		10.37
A75T/P	96.87	-1.40	2.47		-
A75T/P/PC	97.44	1.72	2.47		3.17
A75T/P/BLK	94.86	8.53	3.75		10.91
100T/P	95.84	-1.66	2.87		-
100T/P/PC	96.78	-0.89	4.74		2.23
100T/P/BLK	93.71	9.68	4.24		11.62



deposition methods [36]. As the result of the reaction between  $\text{TiO}_2$  and  $\text{Al}_2\text{O}_3$  in the plasma jet, the tialite phase  $\text{Al}_2\text{TiO}_5$  was formed [37]. This can be observed mostly for the samples A30T/C, A50T/C, and A75T/C. Formation of  $\text{Al}_2\text{TiO}_5$  is considered preferable in the case of photocatalytic processes since it stands out with good light absorption, leading to photocatalytic activity [38].

### 3.3 Surface roughness and wettability

The values for roughness parameters are within the range of 6.90–9.45, 37.67–51.92 and 44.07–66.58  $\mu\text{m}$  for the average roughness of a surface  $R_a$ , maximum peak to valley height  $R_z$  and maximum roughness depth  $R_{\text{max}}$ , respectively. The results showed the disordered directivity of the surface for most of the coatings. The discussed roughness parameters are presented in Table 7. The values of contact angles between almost  $100^\circ$ – $130^\circ$  (Table 8) show that most coatings are hydrophobic. Measurements for samples A15T/C and A05T/C were impossible due to the spilling of water drops on the surface of the coatings. In the case of the rest of the samples, it can be seen that when the surface roughness is greater, the contact angle values also increase. The presented results correspond with the available literature data on the influence of surface roughness on the hydrophobicity of the coating surface. Both in the case of theoretical [39] and laboratory [40] analyses, it was observed that hydrophobicity increases with the increase of surface roughness. This phenomenon can be explained briefly by two mathematical models—Wenzel and Cassie. The Wenzel model assumes that the contact surface increases as roughness rises. This, in turn, causes an increase in effective free

**Table 11** Rate constants and linearly dependent coefficients of Eo degradation in a reaction with the use of powders

Sample	$k$ [1/min]	$R^2$
100T/P	0.0123	0.9964
A75T/P	0.0102	0.9980
A50T/P	0.0076	0.9993
A30T/P	0.0052	0.9983
A15T/P	0.0020	0.9926
A05T/P	0.0011	0.9822
100A/P	0.0009	0.9824

energy at the liquid–solid interface, leading to an enhanced hydrophobicity [41]. According to Cassie’s model, the contact at the liquid–solid interface is created due to air bubbles forming in the rough surface’s depressions, intensifying the hydrophobic effect [42]. In accordance with the literature, the presented parameters can also be related to the catalytic properties of the coatings. Some previously reported research shows that roughness and wettability can strongly influence the photocatalytic performance of different materials in aqueous reaction environments. And so, it can be stated that photocatalytic abilities improve with increasing hydrophobicity and surface roughness [43, 44]. The results obtained in this work indicate the hydrophobicity and high surface roughness of the fabricated  $\text{TiO}_2/\text{Al}_2\text{O}_3$  coatings. It can be expected that they are suitable candidates for conducting photocatalytic processes for removing organic dyes from aqueous solutions.

### 3.4 Light-activated dye degradation and color measurements

Photocatalytic behavior for  $\text{TiO}_2$ ,  $\text{Al}_2\text{O}_3$ , and  $\text{TiO}_2/\text{Al}_2\text{O}_3$ -based powders or coatings was tested in an Eo degradation process. It is well known that  $\text{TiO}_2$  and its blends with  $\text{Al}_2\text{O}_3$  after light irradiation act as catalysts in the process of decomposing organic pollutants from aqueous solutions. As expected, the results show that the efficiency of Eo degradation increases with the increase of  $\text{TiO}_2$  contents in the blends.

Figure 4 presents the decrease in Eo concentration during the processes conducted with the use of powders. In this case, the Eo degradation rate was stated at almost 89, 83, 74, 60, 38, 17, and 14% for 100T/P, A75T/P, A50T/P, A30T/P, A15T/P, A05T/P, and 100A/P, respectively (Table 9). The good efficiency of Eo degradation in the reaction with powders may be caused by the fact that the powders had a high surface area for the reaction in the Eo solution as they were directly added to it and constantly mixed during the process which can influence the enhancement of organic pollutants degradation [45]. However, in the case of reactions carried with powders, some limitations can occur. Literature research indicated that many factors can disturb

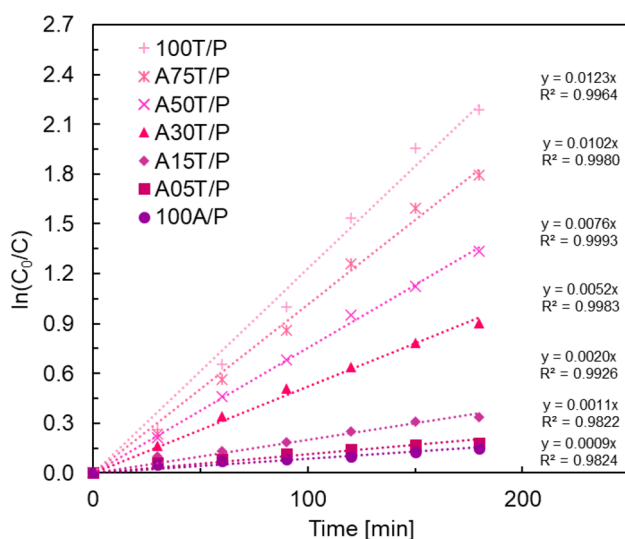


**Fig. 6** Kinetics of Eo degradation in a reaction with the use of powders

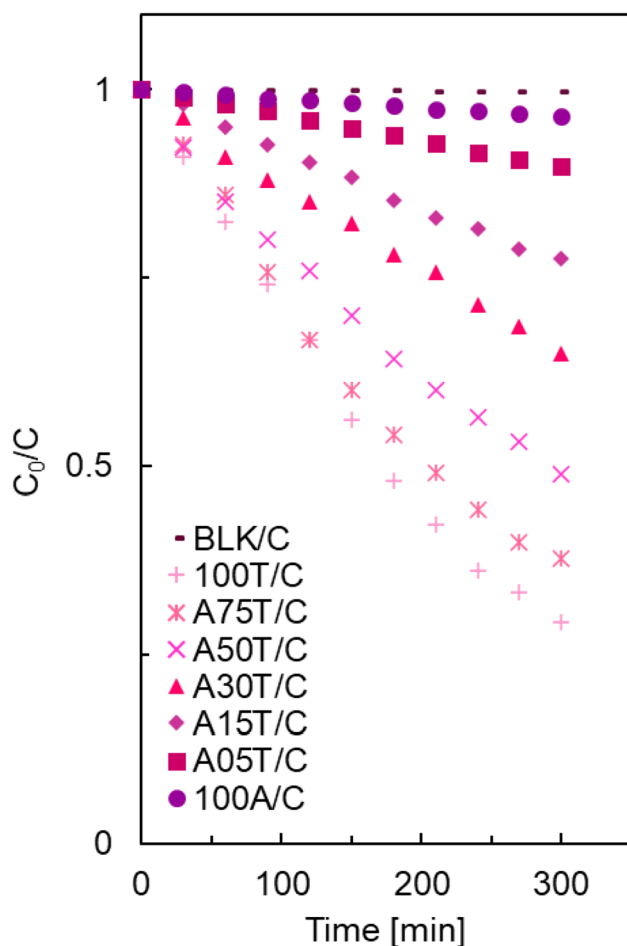


Fig. 7 Decrease in Eo concentration in the reaction with coatings

Table 12 Eo degradation rate in the reaction with coatings

Sample	Eo degradation rate [%]
100T/C	70.71
A75T/C	62.31
A50T/C	51.07
A30T/C	35.11
A15T/C	22.39
A05T/C	10.27
100A/C	3.59

the photocatalysis process. This was first proved by colorimetric analysis. Color measurements before and after the Eo photodegradation process indicate a significant change in the color of the powder. After the process, the color of the powder samples changed from white or white-gray to pink (Table 10), which indicates the adsorption of Eo on their surface. Thus, the  $\Delta E$  value for the powders before and after the process was 2.23, 3.17, 2.93, 6.31, 7.94, 8.96, and 9.07 for 100T/P, A75T/P, A50T/P, A30T/P, A15T/P, A05T/P

and 100A/P, respectively. The recorded differences may suggest partial adsorption of Eo on the surface of the tested powder samples, which can be connected to specific surface area values. Along with the increase in the specific surface area of the tested material, its adsorption capacity increases. This effect has been confirmed in the case of many ceramic materials [46], including  $\text{TiO}_2$  or  $\text{Al}_2\text{O}_3$  powders [47]. Thus, the differences in  $\Delta E$  depending on the powder composition were observed. The values of  $\Delta E$  were lower for the tested samples, with the increasing  $\text{TiO}_2$  content corresponding to the specific surface area results (Table 4). The absorption of Eo on the surface of the powders was also confirmed by dark measurements. The powder samples were stirred in the same reaction conditions (Eo concentration, time, powder addition) without light irradiation. UV-Vis measurement showed a change in the concentration of Eo in the solution and a significant color change in the powders. Here, the UV-Vis investigation showed similar values of the Eo concentration decrease for all tested powder samples (Fig. 5). The Eo concentration after dark tests was stated from 4.02 to 4.20 mg/L. Both with the additional color measurements (Table 10), it was proved that prepared powders hold the ability to absorb dye on their surface. Another bottleneck in the use of powders as photocatalysts is the occurrence of their partial suspension in the tested solutions. This leads to problems with the disruption of the turbidity of tested solutions and their separation and utilization from reaction mixtures [11]. And, even though the tested powder mixtures can significantly influence the high degradation efficiency of Eo, they are also considered to be a contamination.

The rate constants of the processes were determined, knowing that the degradation reaction of Eo from aqueous solutions is a pseudo-first-order reaction [48]. Hence, based on the changes in the concentration of Eo in the solution recorded during the experiments, it was possible to determine the rate constants  $k$  of this reaction carried out in the presence of catalysts in the form of powders or coatings. The analysis was performed using the graphical method based on fitting the experimental data (here, Eo concentration) to the reaction kinetics equation. The reaction rate constant is derived from the linear trend equation:  $y = ax + b$ , where  $k = -a$ . For the Eo degradation processes carried out in this research, plots  $\ln(C_0/C)$  vs. time were drawn. Figure 6 and Table 11 present the results of the kinetic study of the process with the presence of powder samples. The values of linearly dependent coefficients show a good fit of reaction order for almost all of the tested samples. In the case of samples A05T/P and 100A/P, a slight deviation from the linear course was observed. This can be attributed to their poor photocatalytic properties and partial adsorption of the dye on their surface, which could affect the free course of Eo degradation.

**Table 13** Color measurement parameters for coatings before and after Eo degradation (PC—post photodegradation)

Sample	L*	a*	b*	Color	ΔE
100A/C	54.07	-2.49	-9.86		0.22
100A/C/PC	53.94	-2.46	-9.69		
A05T/C	42.66	-2.04	-9.91		0.22
A05T/C/PC	42.78	-2.04	-9.73		
A15T/C	41.18	-1.29	-7.49		1.94
A15T/C/PC	39.26	-1.57	-7.49		
A30T/C	31.30	-0.41	-3.29		0.86
A30T/C/PC	31.65	-0.22	-3.42		
A50T/C	31.10	-0.15	-3.17		0.36
A50T/C/PC	31.37	-0.02	-3.37		
A75T/C	35.08	-0.55	-3.56		1.17
A75T/C/PC	34.11	-0.13	-3.05		
100T/C	34.39	-0.98	-4.49		0.48
100T/C/PC	34.03	-0.70	-4.65		

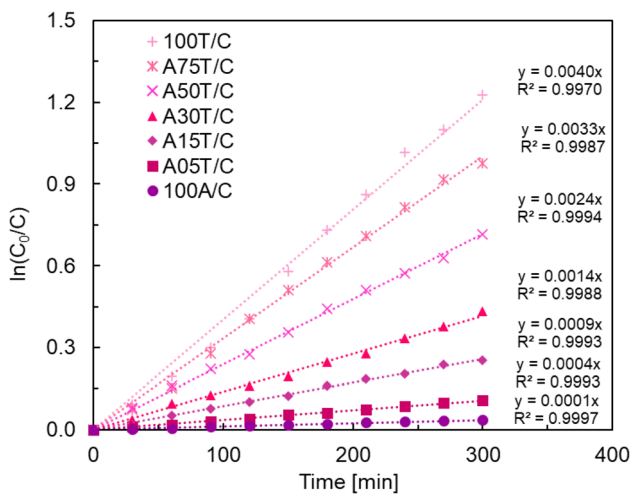


**Fig. 8** Kinetics of Eo degradation in a reaction with the use of coatings

**Table 14** Rate constants and linearly dependent coefficients of Eo degradation in a reaction with the use of coatings

Sample	k [1/min]	R <sup>2</sup>
100T/C	0.0040	0.9970
A75T/C	0.0033	0.9987
A50T/C	0.0024	0.9994
A30T/C	0.0014	0.9988
A15T/C	0.0009	0.9993
A05T/C	0.0004	0.9993
100A/C	0.0001	0.9997

Due to a wide range of limitations related to the practical use of powder materials as photocatalysts, their deposition techniques on solid substrates have been developed for years [49]. In this work, the emphasis on the legitimacy of using coatings as potential catalytic materials in the degradation of organic pollutants was made. Here, plasma-sprayed TiO<sub>2</sub>, Al<sub>2</sub>O<sub>3</sub>, and TiO<sub>2</sub>/Al<sub>2</sub>O<sub>3</sub> coatings were applied as a factor for the photoactivated degradation of Eo. The results show that the efficiency of Eo degradation increases with the increase of TiO<sub>2</sub> contents in the coatings (Fig. 7). The Eo degradation rate (Table 12) was stated at almost 71, 62, 51, 35, 22, 10, and 4% for 100T/C, A75T/C, A50T/C, A30T/C, A15T/C, A05T/C, and 100A/C, respectively.

Compared to commonly produced coatings on steel, coatings that showed the best photocatalytic performance (100T/C, A75T/C or A50T/C) can be considered efficient catalysts in the degradation of organic pollutants from aqueous solutions. In the case of using glass as a substrate, exposure to light is higher, leading to a greater catalytic activity of coatings. This may be due to the better adhesion of ceramic oxides to the glass substrate compared to the steel [50], the increased porosity of the coating, and the transparency of glass, which improves the ability to photo-degrade organic pollutants [51]. It was also proved that the increasing addition of Al<sub>2</sub>O<sub>3</sub> impacted the decrease of the photocatalytic abilities of the prepared materials. Samples A30T/C, A15T/C, A05T/C, and 100A/C showed the lowest efficiency in dye degradation. Despite this, coatings with a higher proportion of Al<sub>2</sub>O<sub>3</sub> may be useful in other catalytic

**Table 15** Exemplar results for photodegradation of organic dyes with the use of TiO<sub>2</sub>-based coatings

Feedstock material/technology	Substrate	Dye	Catalyst dimensions	Reaction conditions	Degradation rate (%)	Refs.
Nano-TiO <sub>2</sub> powder/APS	Stainless steel	MB	1.0×1.0 cm	$t = 2$ h	12	[51]
	FTO glass		1.0×1.0 cm	$C_{\text{dye}} = 5 \times 10^{-5}$ M visible light	25	
Nano-TiO <sub>2</sub> suspension/SPS	Stainless steel	MB	2.5×2.5 cm	$t = 1.5$ h $C_{\text{dye}} = 2 \times 10^{-5}$ M UV-light	44–61	[54]
Nano-TiO <sub>2</sub> suspension/SPS	Stainless steel	MB	2.0×2.0 cm	$t = 6$ h $C_{\text{dye}} = 5$ ppm Visible light	89	[55]
Nano-TiO <sub>2</sub> suspension/SPS	Stainless steel	MB	∅ 3.0 cm	$t = 11$ h $C_{\text{dye}} = 5$ ppm UV-light	~60	[56]
Nano-TiO <sub>2</sub> powder/liquid phase deposition	ITO glass	Eo	n/a	$t = 20$ min $C_{\text{dye}} = 0.1$ mM visible light	78–80	[57]
Nano-TiO <sub>2</sub> /spin coating	Glass	Eo	0.25×0.25 cm	$t = 5$ h $C_{\text{dye}} = 10$ ppm UV-light	88	[58]
Nano-TiO <sub>2</sub> powder/sol-gel	Wool fibers	Eo	n/a	$t = 6$ h $C_{\text{dye}} = 5 \times 10^{-5}$ M UV-light	~70	[59]
Nano-TiO <sub>2</sub> powder/APS	Quartz glass	Eo	19.0×8.0 cm	$t = 6$ h $C_{\text{dye}} = 5$ mg/L UV light	71	This work

processes [52] or as functional materials in various industrial branches [53].

In the case of color measurements for coatings, the  $\Delta E$  values are low, suggesting only a slight color change (Table 13).  $\Delta E$  was 0.48, 1.17, 0.36, 0.86, 1.94, 0.22, and 0.22 for 100T/C, A75T/C, A50T/C, A30T/C, A15T/C, A05T/C and 100A/C, respectively. The colors of the obtained coatings are within the shades of gray—the darkest for the 100T/C sample and the lighter for 100A/C. The coatings' dark color may result from the changes in the crystal phases of TiO<sub>2</sub>, which transforms from anatase to rutile during the APS process, which a color change can accompany due to rapid temperature differences. The color change may also suggest degradation of the polymeric binder PVP upon exposure to high temperatures. Due to the coatings' color, it is impossible to assess whether Eo was adsorbed on the surface of the coatings during the photodegradation process.

Kinetic plots determined for the Eo degradation reaction using coatings as catalysts indicate the correct course of the process (Fig. 8, Table 14). A linear dependence of changes in Eo concentration during the process was observed, and linearly dependent coefficients show a good fit for the data. The expected increase in the reaction rate constant can also be observed with the increase in the share of TiO<sub>2</sub> in the coating composition.

Few reports on light-activated methylene blue (MB) degradation with TiO<sub>2</sub>-based coatings are mentioned in the literature. Nanometric TiO<sub>2</sub> in suspension or powder was used as feedstock material for spraying. Table 15 presents

some results from other works in this matter. It is worth mentioning that the results obtained in other studies cannot be directly compared, mainly due to differences in research methodology. This includes—different reaction conditions, different dyes used as the reference pollutant, or differences in obtaining catalytic coatings.

### 3.5 Scanning electron microscopy

SEM images presented in Fig. 9 show chosen powder samples before and after the photodegradation of Eo. Agglomerates of nanometric particles were observed, confirming the granulation process's effectiveness (Fig. 1). Despite the significant change in the color of the powders after the degradation of Eo, confirmed by color measurements (Table 9), no changes in their morphology were observed during the microscopic analysis.

SEM images of the surfaces of selected coatings before and after the Eo degradation process are presented in Fig. 10. All imaged coatings show an uneven profile as indicated by the arrangement of particles at different levels. The analyzed images show individual nanoparticles as well as their larger agglomerates. An important observation is a difference in the morphology between the coatings obtained by spraying powders with different contents of TiO<sub>2</sub> and Al<sub>2</sub>O<sub>3</sub>. Thus, the image of the 100 T/C sample is dominated by large areas of melted TiO<sub>2</sub> powder, and clusters of smaller particles are visible. These coatings may tend to chip and cohesion due to multiple cracks,

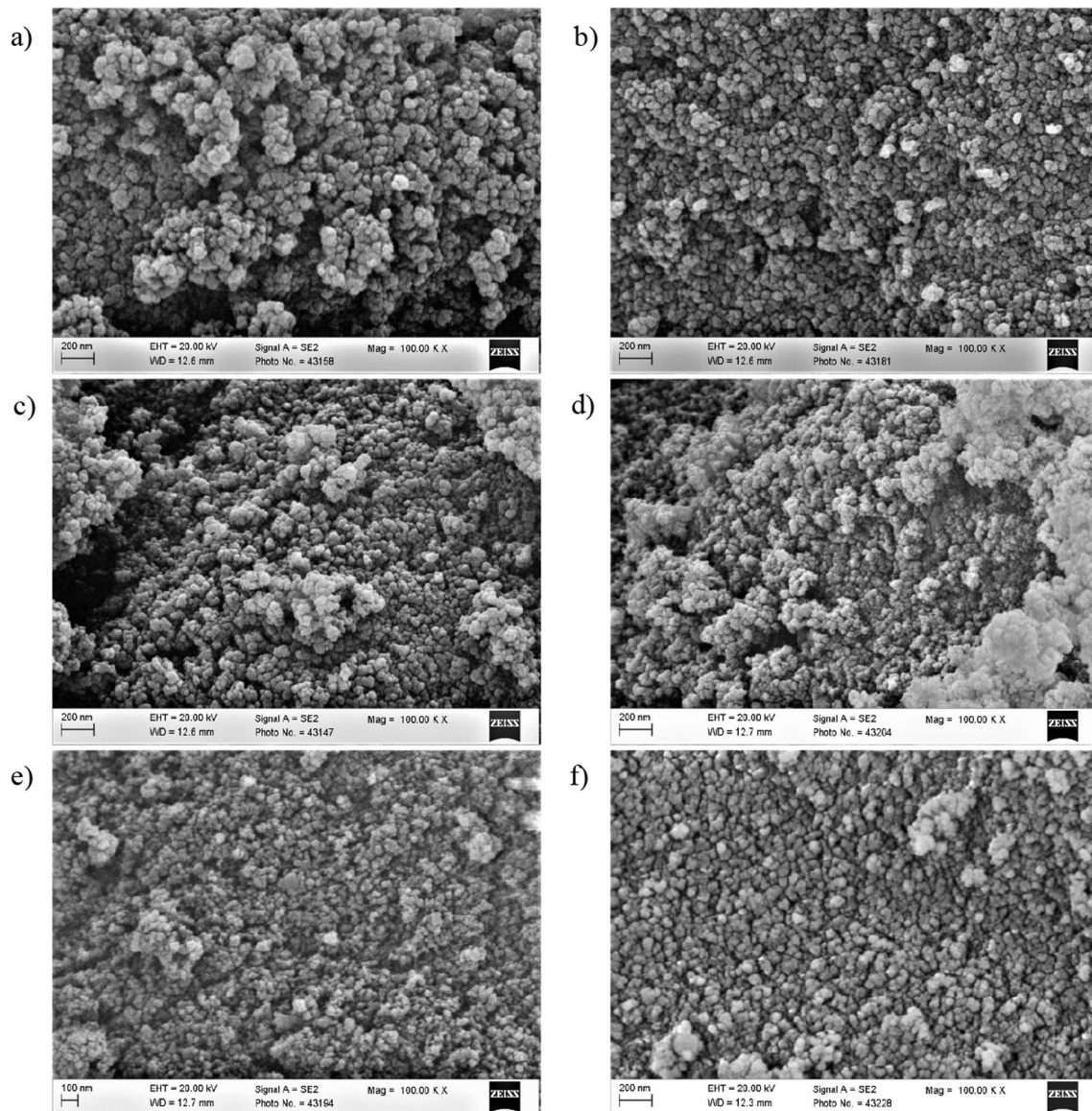


**Fig. 9** SEM images for powder samples before: **a** 100T/P, **c** A50T/P, **e** 100A/P and after: **b** 100T/P/PC, **d** A50T/P/PC, **f** 100A/P/PC Eo photo-degradation

suggesting leakage. The image obtained for the A50T/C sample shows a very different profile. There is a combination of partially melted and fully melted areas. It is worth mentioning that the structure of the imaged coatings is also, to a certain degree, porous, which is confirmed by the voids visible on the surface of the coatings. The craters visible on the surface may suggest that the PVP present in the granules evaporated rapidly under the influence of high temperature during the APS process, which correlates with the colorimetric analysis. They can also result from particles chipping during a sudden significant change in

temperature after the spraying process. The surface of sample 100A/C has the most regular profile. The imaged coating is smooth, and the cracks are not visible. Moreover, melted areas are observed to a large extent on the surface. Single craters can be seen to a lesser extent than for the 100T/C and A50T/C samples. The observed differences may result from the behavior of  $\text{TiO}_2$  and  $\text{Al}_2\text{O}_3$  powders during thermal spray processes, mainly the different nature of phase changes, but also differences in melting points of 1843 and 2072 °C for  $\text{TiO}_2$  and  $\text{Al}_2\text{O}_3$ , respectively. Moreover, no additional damage was observed on the surface of the coatings after photodegradation with Eo, both with the naked eye and during microscopic observation.

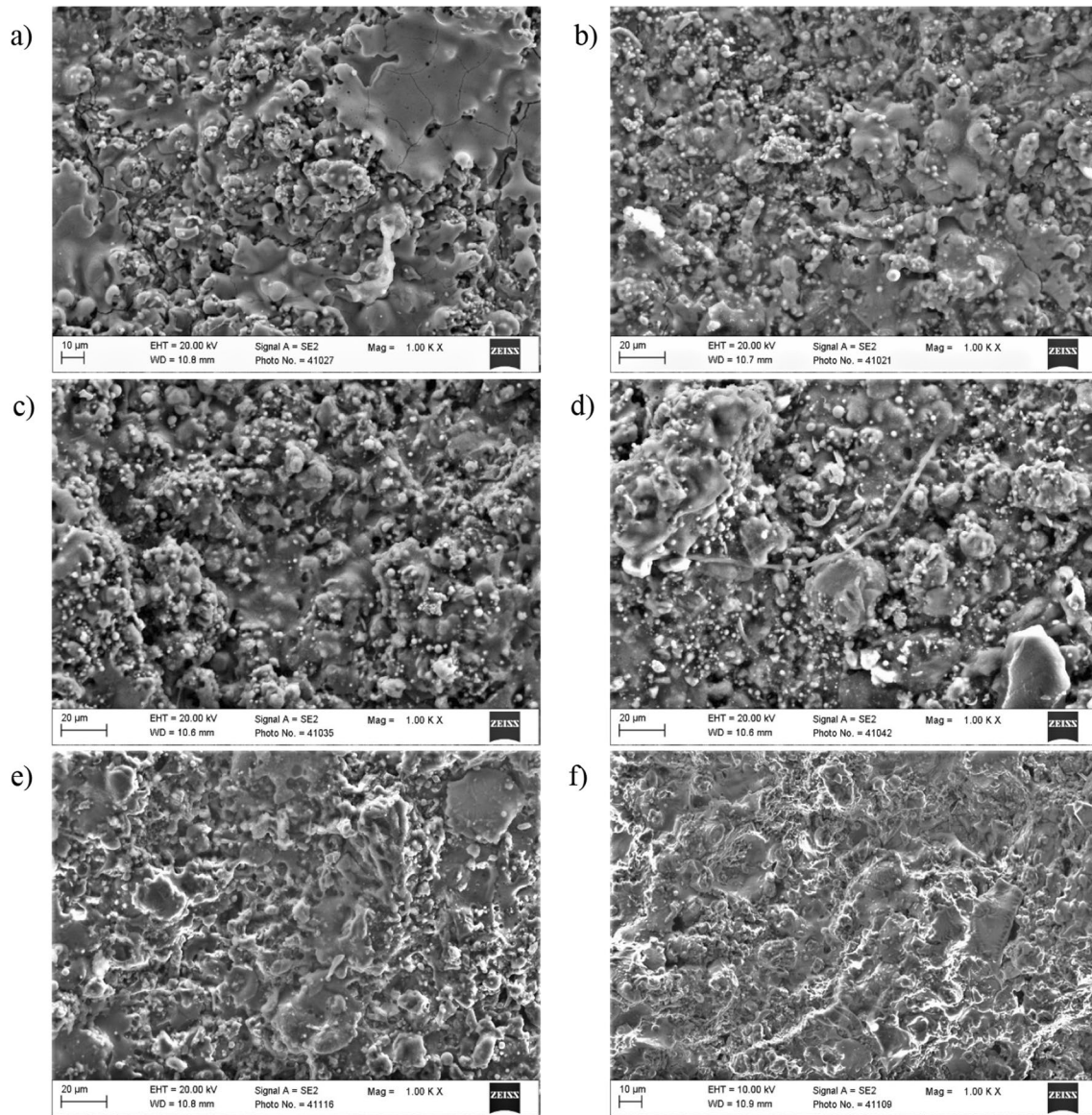


**Fig. 10** SEM images of coatings surface before: **a** 100T/C, **c** A50T/C, **e** 100A/C and after: **b** 100T/C/PC, **d** A50T/C/PC, **f** 100A/C/PC Eo photo-degradation

No blistering, peeling, or cracking of the coatings was noticed. During and after the photodegradation process, there was no visible contamination with any "unfamiliar" additional particles in the test solutions, suggesting the durability of the coatings in the tested environment.

The cross-section of the A50T/C sample presented in Fig. 11 shows the clear boundary between the coating and

the substrate of the tested sample. Moreover, a brittle fracture with a few irregular faults can be observed. The structure of the particles of the sprayed powder after solidification has a morphology most similar to columnar, and numerous locally melted spots are visible on the surface of the tested samples. Discontinuities in the form of pores arising in the manufacturing process may result from imperfections or the

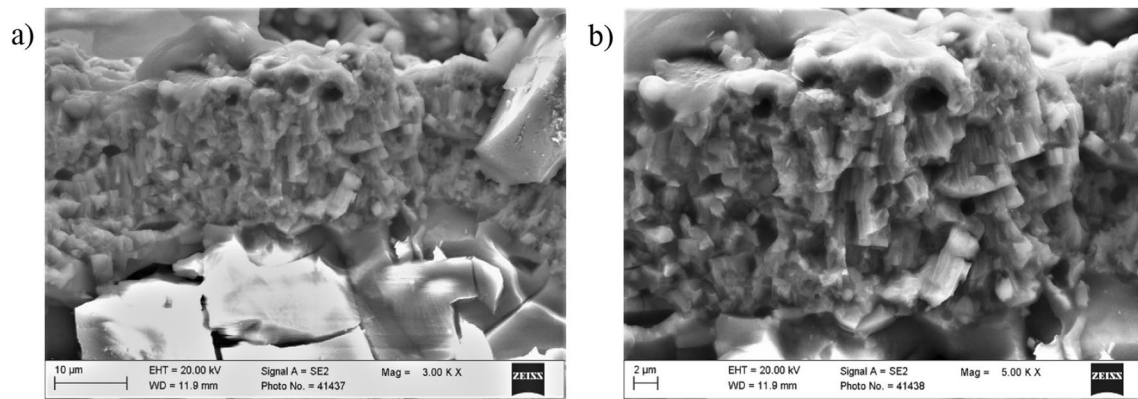


**Fig. 11** SEM images of A50T/C cross section: **a** magnitude  $\times 3000$ , **b** magnitude  $\times 5000$

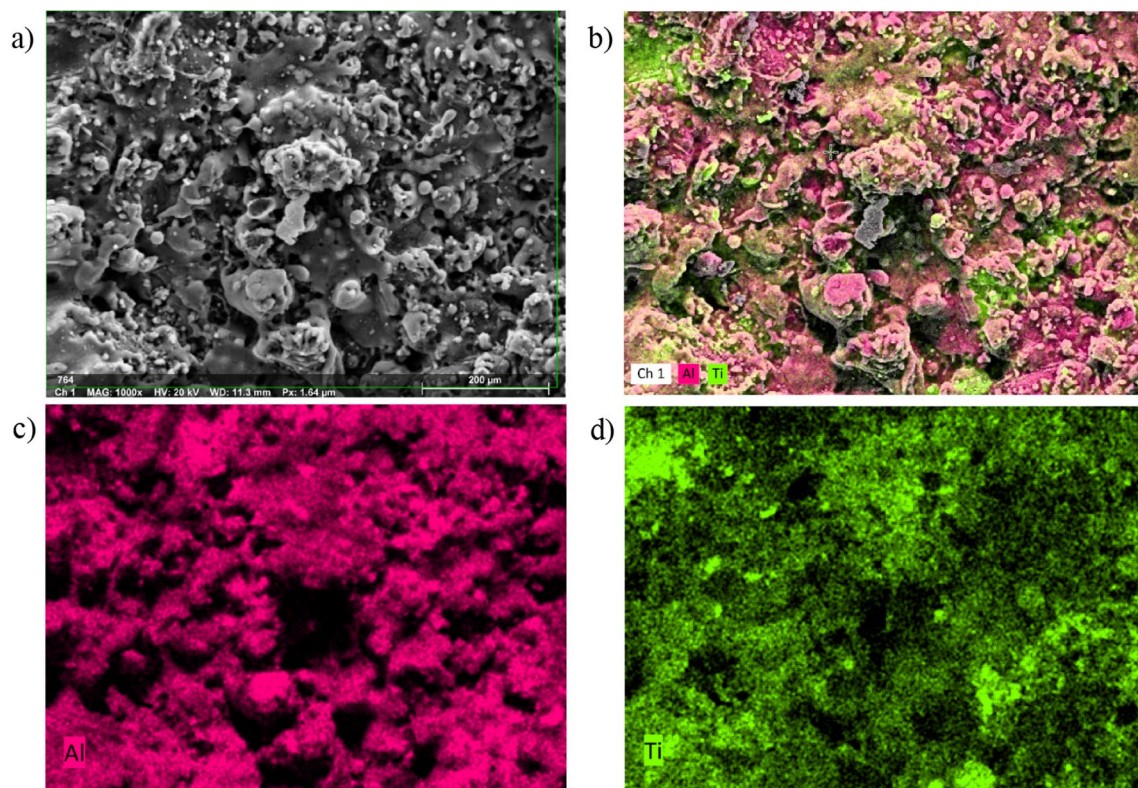


**Fig. 12** SEM image of A50T/C surface (**a**) and elemental distribution for **b** Al, Ti, **c** Al, **d** Ti

accumulation of PVP, which underwent degradation after thermal treatment. The average thickness of the coatings was also determined based on the SEM observations of the samples' cross sections. The following values were determined:  $31.02 \pm 1.91 \mu\text{m}$  (100T/C),  $24.94 \pm 3.08 \mu\text{m}$  (A75T/C),  $29.43 \pm 3.51 \mu\text{m}$  (A50T/C),  $27.55 \pm 4.32 \mu\text{m}$  (A30T/C),  $29.91 \pm 8.40 \mu\text{m}$  (A15T/C),  $30.03 \pm 4.26 \mu\text{m}$  (A05T/C) and  $34.01 \pm 14.84 \mu\text{m}$  (100A/C).

The SEM images presented in Figs. 12 and 13 show the results of the elemental distribution analysis on the example of the surface view and the cross section of the A50T/C sample. The imaging confirmed the presence of all metallic elements coming from the ceramic powders used for the coating fabrication. The distribution of elements is relatively uniform, although it is not devoid of the accumulation of Ti or Al in small areas. Nevertheless, the surface of the analyzed

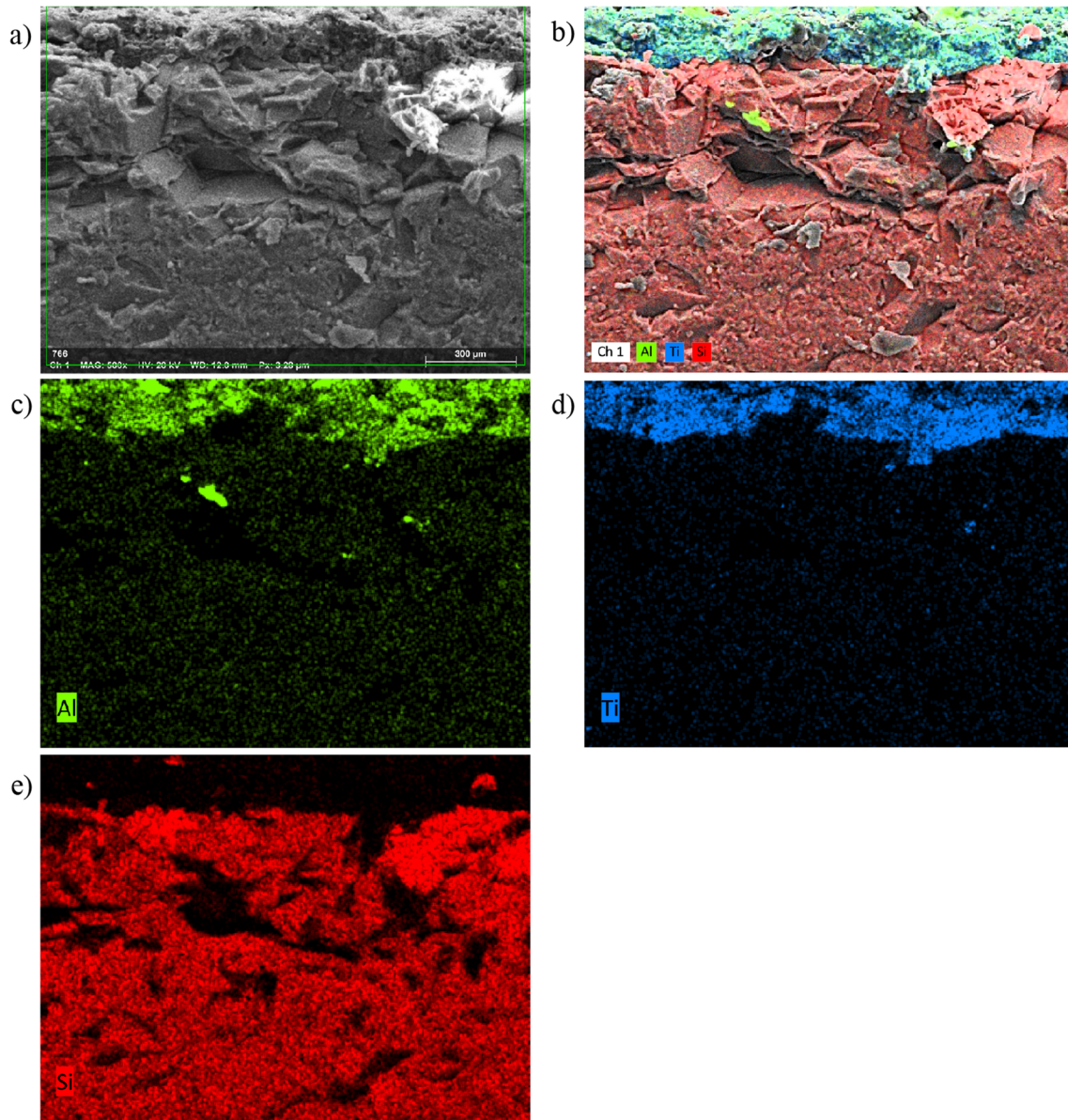


**Fig. 13** SEM image of A50T/C cross-section (a) and elemental distribution for b Al, Ti, Si, c Al, d Ti, e Si

area is predominantly pink, indicating the presence of Al. The distribution of Al and Ti elements at the cross-section is analogous. Here, Si, as the main component of the quartz glass substrate, was also detected. The presented images show a clear boundary of the distribution of the substrate-coating phases.

## 4 Conclusion

Photocatalytic materials hold great potential in various industrial, medical, or pharmaceutical applications. The main direction of processing light-activated compounds is their exploitation as multifunctional coatings. In this research, granulated nanometric  $\text{TiO}_2$ ,  $\text{Al}_2\text{O}_3$ , and  $\text{TiO}_2/\text{Al}_2\text{O}_3$  were deposited on the glass substrate using the APS technology. Catalytic activity was tested in light-activated removal of persistent organic pollutants from aqueous solutions on the example of Eo degradation. The choice



of  $\text{TiO}_2$  and  $\text{Al}_2\text{O}_3$  as photocatalysts was dictated primarily by their functional features, i.e. low toxicity, high thermal stability, or low cost. Moreover, depositing ceramics on glass provides a good combination due to the formation of a well-adhered coating and no need to use additional so-called bond layers traditionally applied on steel substrates.

The following conclusions can be given based on the conducted measurements:

- SEM and physicochemical characterization of powder samples confirmed that the granulation process was effective without significantly affecting the properties of the  $\text{TiO}_2$  and  $\text{Al}_2\text{O}_3$  as delivered. The results of PSD measurements of powders after granulation showed similar distributions for all samples and the mean particle size ( $d_{50}$ ) was stated between 48.42 and 63.28  $\mu\text{m}$ .
- Wettability tests showed that most coatings are hydrophobic, which is advantageous for water treatment applications. These results are consistent with the analysis of the geometric structure of the coatings. The values of the contact angles increased with the surface roughness.
- XRD analysis of the powder samples proved the presence of  $\text{TiO}_2$ , both anatase and rutile and  $\alpha\text{-Al}_2\text{O}_3$ . In the case of the coatings—transformations from anatase to rutile and from  $\alpha\text{-Al}_2\text{O}_3$  into  $\gamma\text{-Al}_2\text{O}_3$  for  $\text{TiO}_2$  and  $\text{Al}_2\text{O}_3$ , respectively, were observed. Moreover, due to the reaction between  $\text{TiO}_2$  and  $\text{Al}_2\text{O}_3$  during the APS process, the  $\text{Al}_2\text{TiO}_5$  tialite phase was formed.
- A relatively high efficiency of Eo degradation for the coatings was confirmed. The highest Eo degradation rate was reached for samples 100T/C, A75T/C, and A50T/C (over 50% and up to 71%).
- Colorimetric analysis before and after the photodegradation process showed a significant color change of the powder samples ( $\Delta E$  2.23–9.07), which may indicate partial adsorption of Eo on the surface of the powders. No significant color changes were observed after the reaction with the coatings.

The use of  $\text{TiO}_2/\text{Al}_2\text{O}_3$  powder samples as photocatalysts is limited on a large scale due to the difficulties in separating them from the post-reaction systems. An effective method for their deposition on glass substrates was proposed, and coatings with photocatalytic activity were obtained. Presented coatings can be applied as architectural materials due to their functionality and decorative effect. Above that, the proposed materials can be used for industrial implementations such as photoreactor cladding, self-cleaning panes, or mountings and fittings for medical and household accessories.

**Acknowledgements** This work was financially supported by the subvention of the Polish Ministry of Education and Science for Łukasiewicz Research Network—Institute of Non-Ferrous Metals for the year 2021.

**Data availability** The authors confirm that all data generated or analysed during the study are included in this published article and are available from the corresponding author on reasonable request.

## Declarations

**Conflict of interest** The authors declare that they have no known competing financial interests or personal relationships that could have appeared to influence the work reported in this paper.

**Research involving human participants and/or animals** This article does not contain any studies with human participants or animals performed by any of the authors.

**Open Access** This article is licensed under a Creative Commons Attribution 4.0 International License, which permits use, sharing, adaptation, distribution and reproduction in any medium or format, as long as you give appropriate credit to the original author(s) and the source, provide a link to the Creative Commons licence, and indicate if changes were made. The images or other third party material in this article are included in the article's Creative Commons licence, unless indicated otherwise in a credit line to the material. If material is not included in the article's Creative Commons licence and your intended use is not permitted by statutory regulation or exceeds the permitted use, you will need to obtain permission directly from the copyright holder. To view a copy of this licence, visit <http://creativecommons.org/licenses/by/4.0/>.

## References

1. Tkaczyk A, Mitrowska K, Posylniak A. Synthetic organic dyes as contaminants of the aquatic environment and their implications for ecosystems: a review. *Sci Total Environ*. 2020. <https://doi.org/10.1016/j.scitotenv.2020.137222>.
2. Dyes & pigments market size, share & trends analysis report by product (pigments, dyes), by application (paints & coatings, printing inks, textiles), By Region (APAC, Europe), And Segment Forecasts. 2021.
3. Shindhal T, Rakholiya P, Varjani S, Pandey A, Ngo HH, Guo W, Yong Ng H, Taherzadeh MJA. A critical review on advances in the practices and perspectives for the treatment of dye industry wastewater. *Bioengineered*. 2021. <https://doi.org/10.1080/21655979.2020.1863034>.
4. Mossavi E, Hosseini SM, Ghaedi M, Azghandi MHA. Adsorption of the azo dyes from wastewater media by a renewable nanocomposite based on the graphene sheets and hydroxyapatite/ZnO nanoparticles. *J Mol Liq*. 2022. <https://doi.org/10.1016/j.molliq.2022.118568>.
5. Nascimento COC, Veit MT, Palácio SM, Gonçalves GC, Fagundes-Klen MR. Combined application of coagulation/flocculation/sedimentation and membrane separation for the treatment of laundry wastewater. *Int J Chem Eng*. 2019. <https://doi.org/10.1155/2019/8324710>.
6. Li J, Gong JL, Zeng GM, Zhang P, Song B, Cao WC, Liu HY, Huan SY. Zirconium-based metal organic frameworks loaded on polyurethane foam membrane for simultaneous removal of dyes with different charges. *J Colloid Interface Sci*. 2018. <https://doi.org/10.1016/j.jcis.2018.05.028>.

7. Shen L, Jin Z, Xu W, Jiang X, Shen YX, Wang Y, Lu Y. Enhanced treatment of anionic and cationic dyes in wastewater through live bacteria encapsulation using graphene hydrogel. *Ind Eng Chem Res.* 2019. <https://doi.org/10.1021/acs.iecr.9b01950>.
8. Alam R, Ardiati FC, Solihat NN, Alam MB, Lee SH, Yanto DHY, Watanabe T, Kim S. Biodegradation and metabolic pathway of anthraquinone dyes by *Trametes hirsuta* D7 immobilized in light expanded clay aggregate and cytotoxicity assessment. *J Hazard Mater.* 2021. <https://doi.org/10.1016/j.jhazmat.2020.124176>.
9. Liu X, Chen Z, Du W, Liu P, Zhang L, Shi F. Treatment of wastewater containing methyl orange dye by fluidized three dimensional electrochemical oxidation process integrated with chemical oxidation and adsorption. *J Environ Manag.* 2022. <https://doi.org/10.1016/j.jenvman.2022.114775>.
10. Rajendrachari S, Taslimi P, Karaoglanli AC, Uzun O, Alp E, Jayaprakash GK. Photocatalytic degradation of Rhodamine B (RhB) dye in waste water and enzymatic inhibition study using cauliflower shaped ZnO nanoparticles synthesized by a novel One-pot green synthesis method. *Arab J Chem.* 2021. <https://doi.org/10.1016/j.arabjc.2021.103180>.
11. Saeed M, Muneer M, Haq A, Akram N. Photocatalysis: an effective tool for photodegradation of dyes—a review. *Environ Sci Pollut Res.* 2022. <https://doi.org/10.1007/s11356-021-16389-7>.
12. Kumari A, Chaudhary DR. Engineered microbes and evolving plastic bioremediation technology. *Bioremediat Pollut.* 2020. <https://doi.org/10.1016/B978-0-12-819025-8.00021-1>.
13. Thandu M, Comuzzi C, Goi D. Phototreatment of water by organic photosensitizers and comparison with inorganic semiconductors. *Int J Photoenergy.* 2015. <https://doi.org/10.1155/2015/521367>.
14. Pelaez M, Nolan NT, Pillai SC, Seery MK, Falaras P, Kontos AG, Dunlop PSM, Hamilton JWJ, Byrne JA, O'Shea K, Entezari MH, Dionysiou DD. A review on the visible light active titanium dioxide photocatalysts for environmental applications. *Appl Catal B Environ.* 2012. <https://doi.org/10.1016/j.apcatb.2012.05.036>.
15. Zhang J, Xu Q, Feng Z, Li M, Li C. Importance of the relationship between surface phases and photocatalytic activity of TiO<sub>2</sub>. *Angew Chem.* 2008. <https://doi.org/10.1002/ange.200704788>.
16. Zhang J, Zhou P, Liu J, Yu J. New understanding of the difference of photocatalytic activity among anatase, rutile and brookite TiO<sub>2</sub>. *Phys Chem Chem Phys.* 2014. <https://doi.org/10.1039/C4CP02201G>.
17. Hanaor DAH, Sorrell CC. Review of the anatase to rutile phase transformation. *J Mater Sci.* 2015. <https://doi.org/10.1524/zkri.1972.136.16.273>.
18. Klyatskina E, Rayón E, Darut G, Salvador MD, Sánchez E, Montavon G. A study of the influence of TiO<sub>2</sub> addition in Al<sub>2</sub>O<sub>3</sub> coatings sprayed by suspension plasma spray. *Surf Coat Technol.* 2015. <https://doi.org/10.1016/j.surfcoat.2015.07.029>.
19. Khaskhoussi A, Calabrese L, Bouaziz J, Proverbio E. Performances and aging stability of new Al<sub>2</sub>O<sub>3</sub>-ZrO<sub>2</sub>-TiO<sub>2</sub> ternary ceramic composites. *Mater Chem Phys.* 2020. <https://doi.org/10.1016/j.matchemphys.2019.122586>.
20. Yoo SM, Lee SY, Kim G, Hernandez EV, Mora-Sero I, Yoon SJ, Shin T, Lee SH, Ahn S, Song MK, Kim M, Lee HJ. Preparation of nanoscale inorganic CsPbI<sub>3</sub>Br<sub>3-x</sub> perovskite photosensitizers on the surface of mesoporous TiO<sub>2</sub> film for solid-state sensitized solar cells. *Appl Surf Sci.* 2021. <https://doi.org/10.1016/j.apsusc.2021.149387>.
21. Gibas A, Baszczuk A, Jasiorski M, Winnicki M, Ociński D. Preparation of visible-light active oxygen-rich TiO<sub>2</sub> coatings using low pressure cold spraying. *Coatings.* 2022. <https://doi.org/10.3390/coatings12040475>.
22. Chebanenko MI, Lebedev LA, Ugolkov VL, Prasolov ND, Nevedomskiy VN. Chemical and structural changes of g-C<sub>3</sub>N<sub>4</sub> through oxidative physical vapor deposition. *Appl Surf Sci.* 2022. <https://doi.org/10.1016/j.apsusc.2022.154079>.
23. Ehsan MA, Naem R, McKee V, Rehman A, Hakeem AS, Mazhar M. Fabrication of photoactive CaTiO<sub>3</sub>-TiO<sub>2</sub> composite thin film electrodes via facile single step aerosol assisted chemical vapor deposition route. *J Mater Sci Mater Electron.* 2019. <https://doi.org/10.1007/s10854-018-0411-4>.
24. Roata IC, Croitoru C, Pascu A, Stanciu EM. Photocatalytic coatings via thermal spraying: a mini-review. *AIMS Mater Sci.* 2019. <https://doi.org/10.3934/matserci.2019.3.335>.
25. Toma FL, Alamri S, Leupolt B, Kunze T, Barbosa M. Functionalization of suspension sprayed HVOF TiO<sub>2</sub> coatings by direct laser interference patterning. *J Therm Spray Technol.* 2021. <https://doi.org/10.1007/s11666-021-01181-3>.
26. Bozorgtabar M, Rahimipour M, Salehi M, Jafarpour M. Structure and photocatalytic activity of TiO<sub>2</sub> coatings deposited by atmospheric plasma spraying. *Surf Coat Technol.* 2011. <https://doi.org/10.1016/j.surfcoat.2011.03.045>.
27. Khatibnezhad H, Ambriz-Vargas F, Ben EF, Moreau C. An investigation on the photocatalytic activity of sub-stoichiometric TiO<sub>2-x</sub> coatings produced by suspension plasma spray. *J Eur Ceram.* 2021. <https://doi.org/10.1016/j.jeurceramsoc.2020.08.017>.
28. Ozkan E, Allan E, Parkin IP. White-light-activated antibacterial surfaces generated by synergy between zinc oxide nanoparticles and crystal violet. *ACS Omega.* 2018. <https://doi.org/10.1021/acsomega.7b01473>.
29. Deshmukh SP, Koli VB, Dhodamani AG, Patil SM, Ghodake VS, Delekar SD. Ultrasonochemically modified Ag@TiO<sub>2</sub> nanocomposites as potent antibacterial agent in the paint formulation for surface disinfection. *ChemistrySelect.* 2021. <https://doi.org/10.1002/slct.202002903>.
30. Akarsu E, Uslu R. Light-activated hybrid organic/inorganic antimicrobial coatings. *J Sol-Gel Sci Technol.* 2018. <https://doi.org/10.1007/s10971-018-4714-y>.
31. Zhai W, Bai L, Zhou R, Fan X, Kang G, Liu Y, Zhou K. Recent progress on wear-resistant materials: designs, properties, and applications. *Adv Sci.* 2021. <https://doi.org/10.1002/advs.202003739>.
32. Musalek R, Tesar T, Dudik J, Medricky J, Cech J, Lukac F. Cohesion of dissimilar splats in hybrid plasma-sprayed coatings: a case study for Al<sub>2</sub>O<sub>3</sub>-TiO<sub>2</sub>. *J Therm Spray Technol.* 2022. <https://doi.org/10.1007/s11666-022-01401-4>.
33. Pawlowski L. Finely grained nanometric and submicrometric coatings by thermal spraying: a review. *Surf. Coat Technol.* 2008. <https://doi.org/10.1016/j.surfcoat.2008.04.004>.
34. Vicent M, Sánchez E, Mallo G, Moreno R. Study of colloidal behaviour and rheology of Al<sub>2</sub>O<sub>3</sub>-TiO<sub>2</sub> nanosuspensions to obtain free-flowing spray-dried granules for atmospheric plasma spraying. *Ceram Int.* 2013. <https://doi.org/10.1016/j.ceramint.2013.03.083>.
35. Fernandes MacHado NRC, Santana VS. Influence of thermal treatment on the structure and photocatalytic activity of TiO<sub>2</sub> P25. *Catal Today.* 2005. <https://doi.org/10.1016/j.cattod.2005.07.022>.
36. Utu ID, Marginean G, Hulka I, Serban VA, Cristea D. Properties of the thermally sprayed Al<sub>2</sub>O<sub>3</sub>-TiO<sub>2</sub> coatings deposited on titanium substrate. *Int J Refract Met Hard Mater.* 2015. <https://doi.org/10.1016/j.ijrmhm.2015.03.009>.
37. Michalak M, Toma FL, Latka L, Sokołowski P, Barbosa M, Ambroziak A. A study on the microstructural characterization and water-based suspensions. *Materials.* 2020. <https://doi.org/10.3390/ma13112638>.

38. Azarniya A, Soltaninejad M, Zekavat M, Bakhshandeh F, Hosseini HRM, Amutha C, Ramakrishna S. Application of nanostructured aluminium titanate ( $\text{Al}_2\text{TiO}_5$ ) photocatalyst for removal of organic pollutants from water: influencing factors and kinetic study. *Mater Chem Phys*. 2020. <https://doi.org/10.1016/j.matchemphys.2020.123740>.
39. Yang C, Tartaglino U, Persson BNJ. Influence of surface roughness on superhydrophobicity. *Phys Rev Lett*. 2006. <https://doi.org/10.1103/PhysRevLett.97.116103>.
40. Wang J, Wu Y, Cao Y, Li G, Liao Y. Influence of surface roughness on contact angle hysteresis and spreading work. *Colloid Polym Sci*. 2020. <https://doi.org/10.1007/s00396-020-04680-x>.
41. Wenzel RN. Resistance of solid surfaces to wetting by water. *Ind Eng Chem Res*. 1936. <https://doi.org/10.1021/ie50320a024>.
42. Cassie ABD, Baxter S. Wettability of porous surfaces. *Trans Faraday Soc*. 1944. <https://doi.org/10.1039/TF9444000546>.
43. Hosseini ZS, Haghparast F, Masoudi AA, Mortezaali A. Enhanced visible photocatalytic performance of un-doped  $\text{TiO}_2$  nanoparticles thin films through modifying the substrate surface roughness. *Mater Chem Phys*. 2022. <https://doi.org/10.1016/j.matchemphys.2021.125530>.
44. Upadhaya D, Kumar TP, Purkayastha DD. Tuning the wettability and photocatalytic efficiency of heterostructure  $\text{ZnOSnO}_2$  composite films with annealing temperature. *Mater Sci Semicond*. 2019. <https://doi.org/10.1016/j.mssp.2019.02.009>.
45. Nosaka Y, Nosaka AY. Generation and detection of reactive oxygen species in photocatalysis. *Chem Rev*. 2017. <https://doi.org/10.1021/acs.chemrev.7b00161>.
46. Yan S, Pan Y, Wang L, Liu J, Zhang Z, Huo W, Yang J, Huang Y. Synthesis of low-cost porous ceramic microspheres from waste gangue for dye adsorption. *J Adv Ceram*. 2017. <https://doi.org/10.1007/s40145-017-0253-1>.
47. Guo N, Liang Y, Lan S, Liu L, Ji G, Gan S, Zou H, Xu X. Uniform  $\text{TiO}_2$ - $\text{SiO}_2$  hollow nanospheres: synthesis, characterization and enhanced adsorption-photodegradation of azo dyes and phenol. *Appl Surf Sci*. 2014. <https://doi.org/10.1016/j.apsusc.2014.03.136>.
48. Poullos I, Micropoulou E, Panou R, Kostopoulou E. Photooxidation of eosin Y in the presence of semiconducting oxides. *Appl Catal B Environ*. 2003. [https://doi.org/10.1016/S0926-3373\(02\)00160-1](https://doi.org/10.1016/S0926-3373(02)00160-1).
49. Mak CH, Han X, Du M, Kai JJ, Tsang KF, Jia G, Cheng KC, Shenk HH, Hsu HY. Heterogenization of homogeneous photocatalysts utilizing synthetic and natural support materials. *J Mater Chem A*. 2021. <https://doi.org/10.1039/D0TA08334H>.
50. Hosseini SN, Borghei SM, Vossoughi M, Taghavinia N. Immobilization of  $\text{TiO}_2$  on perlite granules for photocatalytic degradation of phenol. *Appl Catal B Environ*. 2007. <https://doi.org/10.1016/j.apsusc.2006.12.015>.
51. Zhang C, Chaudhary U, Das S, Godavarty A, Agarwal A. Effect of porosity on photocatalytic activity of plasma-sprayed  $\text{TiO}_2$  coating. *J Therm Spray Technol*. 2013. <https://doi.org/10.1007/s11666-013-9964-1>.
52. Mehla S, Das J, Jampaiah D, Periasamy S, Nafady A, Bhargav SK. Recent advances in preparation methods for catalytic thin films and coatings. *Catal Sci*. 2019. <https://doi.org/10.1039/C9CY00518H>.
53. Garg P, Jamwal A, Kumar D, Sadasivuni KK, Hussaind CM, Gupta P. Advance research progresses in aluminium matrix composites: manufacturing & applications. *J Mater Res Technol*. 2019. <https://doi.org/10.1016/j.jmrt.2019.06.028>.
54. Hosseinabadi N, Dehghanian HA.  $\text{TiO}_2$  photocatalytic ultrafiltration membrane developed with suspension plasma spray process. *Suspens Plasma Spray Coat Adv Ceram*. 2022. <https://doi.org/10.3390/coatings12111764>.
55. Zhai M, Liu Y, Huang J, Wang Y, Chen K, Fu Y, Li H. Efficient suspension plasma spray fabrication of black titanium dioxide coatings with visible light absorption performances. *Ceram Int*. 2019. <https://doi.org/10.1016/j.ceramint.2018.09.268>.
56. Liu X, Wen K, Deng C, Yang K, Deng C, Liu M, Zhou K. Nanostructured photocatalytic  $\text{TiO}_2$  coating deposited by suspension plasma spraying with different injection positions. *J Therm Spray Technol*. 2018. <https://doi.org/10.1007/s11666-018-0693-3>.
57. Pato AH, Balouch A, Talpur FN, Abdullah PP, Mahar AM, Jagirani MS, Kumar S, Sanam S. Fabrication of  $\text{TiO}_2$ @ITO-grown nanocatalyst as efficient applicant for catalytic reduction of Eosin Y from aqueous media. *Environ Sci Pollut*. 2021. <https://doi.org/10.1007/s11356-020-10548-y>.
58. Hernández-Del Castillo PC, Oliva J, Robledo-Trujillo G, Rodríguez-González V. Enhancing the eosin-yellowish dye degradation in drinking water by using  $\text{TiO}_2$  coatings co-doped with Ni and In. *Environ Sci Pollut*. 2023. <https://doi.org/10.1007/s11356-022-22572-1>.
59. Moafi HF, Shojaie AF, Zanjanchi MA. The comparison of photocatalytic activity of synthesized  $\text{TiO}_2$  and  $\text{ZrO}_2$  nanosize onto wool fibers. *Appl Surf Sci*. 2010. <https://doi.org/10.1016/j.apsusc.2010.02.022>.

**Publisher's Note** Springer Nature remains neutral with regard to jurisdictional claims in published maps and institutional affiliations.

## Authors and Affiliations

Alicja Duda<sup>1,3</sup>  · Bartosz Kopyciński<sup>2,3</sup> · Łukasz Hawelek<sup>1</sup> · Marcin Lis<sup>1</sup> · Grzegorz Muzia<sup>1</sup> · Adriana Wrona<sup>1</sup>

✉ Alicja Duda  
alicja.duda@imn.lukasiewicz.gov.pl

<sup>1</sup> Łukasiewicz Research Network-Institute of Non-Ferrous Metals, Sowińskiego 5 St., 44-100, Gliwice, Poland

<sup>2</sup> Łukasiewicz Research Network-Institute for Engineering of Polymer Materials and Dyes, Marii Skłodowskiej-Curie 55 St., 87-100, Toruń, Poland

<sup>3</sup> Doctoral School, Silesian University of Technology, Akademicka 2A St., 44-100, Gliwice, Poland